

Limali Sahoo, S. Bhuyan, S.N. Das\*

Faculty of Engineering and Technology (ITER), Siksha 'O' Anusandhan (Deemed to be University), Bhubaneswar 751030, India

\*Corresponding author. E-mail: satyaprakashdas@soa.ac.in

Received (Otrzymano) 19.04.2023

## TIN OXIDE-TITANIA BASED ELECTRONIC SYSTEM: SYNTHESIS, STRUCTURAL, MICROSTRUCTURAL AND DIELECTRIC PROPERTIES

$\text{SnO}_2\text{-TiO}_2$ , a composite ceramic electronic element was produced by employing a cost-effective and reliable method known as the solid-state synthesis process. The phase, microstructure, chemical composition, and electrical characteristics across a wide frequency range of 1 kHz-1 MHz were evaluated in detail to comprehend this electronic candidate as a capacitive component. The XRD study revealed a polycrystalline tetragonal structure with a crystallite size of 57.9 nm. The SEM micrograph revealed uniformly distributed grains and the calculated average grain size is 0.199  $\mu\text{m}$ . A hydrophilic porous nature was also ascertained from the SEM micrograph. A high dielectric constant (2623) with low dielectric loss (7.5) resulted at the 1 kHz frequency and 400°C. The enhanced capacitive nature was determined by impedance spectroscopy under an extensive frequency and temperature range. The mechanism and nature of conduction at various temperatures were ascertained from the conductivity analysis. The electric modulus characteristics substantiate the non-Debye relaxation of this composite. Based on the comprehensive results, the synthesized component can have prospective applications as a capacitive component for humidity sensors and other electronic devices.

**Keywords:** impedance spectroscopy, non-Debye, solid-state, porous microstructure, electrical properties

### INTRODUCTION

Oxide ceramics have indeed been a subject of significant interest and research across the fields of material science and electronic applications for several years because of their excellent mechanical and corrosion resistance, with good physicochemical stability and dielectric properties in optical, electronics, environmental, and biomedical sectors [1-7]. Moreover, ceramic oxides can withstand the toughest industrial environments with maintained stability. The combination of a porous microstructure as well as surface reactivity with moisture in oxide ceramics makes them a highly promising and effective choice for humidity sensor applications [8, 9]. The qualities of ceramic oxides are shaped by various factors, encompassing the quality of the raw material, the chemical composition, processing methods, temperature, sintering conditions, and particle characteristics. Tin oxide ( $\text{SnO}_2$ ) and titania ( $\text{TiO}_2$ ) are two popularly reported ceramics with a vast range of applications in different fields of science.

$\text{SnO}_2$  possesses distinctive molecular and electrical properties a simple structure with necessary functionalities, long-term stability, strong adsorption capability, an active surface area, and it is inexpensive. These beneficial characteristics of  $\text{SnO}_2$  are exploited in humidity sensor applications [10-15]. Moreover, the high optical permeability and high bandgap (about

3.6 eV) of  $\text{SnO}_2$  at room temperature make it a favorable component for applications in the optical field [16]. However, low response, poor linearity, and long recovery time are the inherent drawbacks generated due to oxygen vacancies in intrinsic  $\text{SnO}_2$  [17, 18]. Hence, to increase the efficiency and performance of intrinsic  $\text{SnO}_2$ -based components, mixed oxide or doping techniques are often implemented [19]. In order to mitigate the drawbacks of pure  $\text{SnO}_2$ , it is often doped with  $\text{TiO}_2$ . Its high availability, low toxicity, high chemical and thermal stability, strong oxidizing capacity, and economically efficiency are some remarkable aspects of  $\text{TiO}_2$  [11, 20].  $\text{TiO}_2$  is available in three crystalline forms; rutile, brookite, and anatase [21]. The easy and simple fabrication process of  $\text{TiO}_2$  makes it a commonly used sensing element in research applications. The excellent electrical, optical, physical, and chemical properties of  $\text{TiO}_2$  are utilized in humidity sensor design [9, 22].

$\text{TiO}_2$  is a popular choice for designing high-performance humidity sensors because of its porous microstructure, hydrophilic characteristics, large surface area, suitable pore size distribution, and pore volume, which delivers a more active path of surface for the adsorption of water molecules, and therefore exhibits high sensitivity towards humidity [23, 24].

This paper demonstrates a reliable and simple solid-state reaction method for preparing a  $\text{SnO}_2\text{-TiO}_2$  composite. The  $\text{SnO}_2\text{-TiO}_2$  composite of an electronic material system  $[(\text{Sn}_x\text{Ti}_{1-x})\text{O}_2]$  with a stoichiometric composition of  $x = 0.2$  was chosen to synthesize the  $(\text{Sn}_{0.2}\text{Ti}_{0.8})\text{O}_2$  ceramic component. The material was produced with a 20:80 molecular wt.% of  $\text{SnO}_2$  and  $\text{TiO}_2$ , respectively. The wt.% of  $\text{TiO}_2$  is more than  $\text{SnO}_2$  to enhance the hydrophilicity characteristics of the developed product, which can be exploited in humidity sensors. The XRD study revealed the structure, whereas SEM was carried out for microstructural analysis. The electrical analysis, which included dielectric, impedance, conductivity, and modulus study, was conducted by means of an LCR analyzer. With its large surface area, the prepared composite can facilitate the occurrence of additional surface oxygen vacancies, which helps the adsorption of more moisture to elevate the humidity-sensing action.

## EXPERIMENTAL PART

The synthesis of the ceramic composite  $(\text{Sn}_{0.2}\text{Ti}_{0.8})\text{O}_2$  was performed by means of a simple and economical solid-state ceramic method [25, 26]. This method involves several intermediate annealing as well as milling steps to achieve a homogeneous mixture product. The raw oxide powders ( $\text{SnO}_2$  &  $\text{TiO}_2$ , purity more than 99.9%, Loba Chemicals Pvt. Ltd., India) were precisely weighed utilizing a Mettler digital balance with an exact stoichiometric ratio (20:80 molecular weight). In the first step, the two weighed oxide powders were dry milled thoroughly for 4-5 h and subsequently grinding was performed in a wet medium for 5 h (an addition of 75 mL of 70 vol.% absolute methanol) to obtain a homogeneous mixed powder. Thereafter, the prepared powder was calcined for four hours at  $950^\circ\text{C}$ . Then the produced powder was again ground thoroughly to prepare fine nano-particles for X-ray diffraction study (XRD, Rigaku H12 Ultima-IV,  $\lambda = 1.5406 \text{ \AA}$ , step size = 0.02, scan rate  $2^\circ/\text{min}$ , and range =  $20^\circ$  to  $80^\circ$ ). The XRD data helps to evaluate the phase and crystallinity of the synthesized sample. Then polyvinyl alcohol (PVA, binder) was added to the calcined powder thoroughly for pellet preparation. Under a pressure of 4 MPa, circular pellets of approximately 10 mm  $\times$  2 mm were prepared using a hydraulic press. Once the pellets were ready, the sintering process was carried out at  $980^\circ\text{C}$  for a duration of 4 h. In the next step, both surfaces of the pellets were polished with sandpaper to create a parallel plane. To record various electrical components (capacitance, loss, phase, and impedance), the deposition of a silver paste (electrode) was made on both sides of the pellet. Different electrical investigations were performed utilizing an LCR analyzer (ZM-2376, NF Corporation) at extensive temperature ( $35\text{-}450^\circ\text{C}$ ) and frequency (1 kHz-1 MHz) ranges. The flowchart of the synthesis procedure is presented in Figure 1.

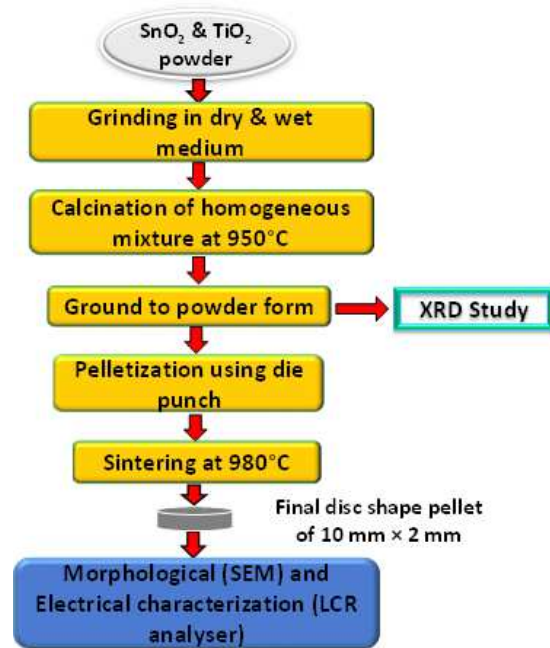


Fig. 1. Process steps for synthesis of  $(\text{Sn}_{0.2}\text{Ti}_{0.8})\text{O}_2$

## RESULTS AND DISCUSSION

### Structural investigation

XRD analysis (at room temperature) was performed to identify the crystallinity of the prepared composite  $(\text{Sn}_{0.2}\text{Ti}_{0.8})\text{O}_2$ . X'Pert HighScore Plus was used to index the principal sharp XRD peaks, and the tetragonal crystal structure of the composite was reported. The reflection peaks of (110), (011), (020), (121), (220), (002), (130), (112), (031), (022), and (231) indicate the cassiterite phase of  $\text{SnO}_2$  (Reference code: 98-001-7011). Similarly, the reflection peaks of (110), (011), (020), (111), (121), (220), (002), and (031) show the anatase phase of  $\text{TiO}_2$  (Reference Code: 98-000-5224). The collected lattice parameters of the cassiterite phase are  $a = 4.7360 \text{ \AA}$ ,  $b = 4.7360 \text{ \AA}$ ,  $c = 3.1850 \text{ \AA}$ , and  $v = 71.44 \text{ \AA}^3$ . Likewise, in the anatase phase, the observed lattice parameters are  $a = 3.7840 \text{ \AA}$ ,  $b = 3.7840 \text{ \AA}$ ,  $c = 9.5150 \text{ \AA}$ , and  $v = 136.24 \text{ \AA}^3$ . The average crystallite size  $C$ , dislocation density  $\mu$ , and lattice strain  $\chi$  were determined to be 57.9 nm,  $2.98 (10^{14} \text{ m}^{-2})$ , and  $1.518 \times 10^{-3}$  by using Equation (1) (Debye-Scherrer's formula) [27], Equation (2) [28] and Equation (3) [20], respectively:

$$C = \frac{K\lambda}{\beta \cos \theta} \quad (1)$$

$$\mu = \frac{1}{C^2} \quad (2)$$

$$\chi = \frac{\beta}{4 \tan \theta} \quad (3)$$

where,  $K$ ,  $\lambda$ , and  $\beta$  are the Scherer factor (i.e. 0.9), X-ray wavelength, and full width at half maximum, respectively.

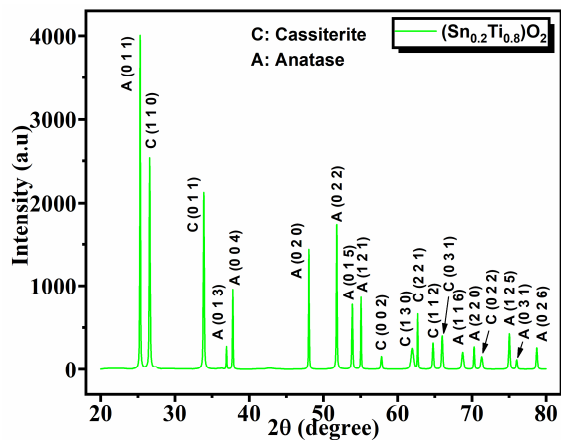


Fig. 2. XRD pattern of  $(\text{Sn}_{0.2}\text{Ti}_{0.8})\text{O}_2$

### Microstructural study

The microstructural analysis of the prepared composite was conducted using the SEM micrograph (Fig. 3a). The distribution of grains with non-uniform sizes was observed by SEM (model: Evo 18). The SEM micrograph of this material suggests the presence of a highly porous microstructure that could be suitable for water molecules to adsorb onto the sample surface. The grain distribution histogram of the prepared component is presented in Figure 3b. By using Image J software, the evaluated average grain size was found to be  $0.199 \mu\text{m}$ . Compositional analysis was conducted by means of EDAX, the spectrum of which is presented in Figure 3c. The presence of all the elemental components (Sn, Ti, and O) without any impurity was confirmed from the EDAX spectrum. The practical and

calculated weight percentages of all the elements present in the composite are given in Table 1 for better comparative analysis.

TABLE 1. Elemental composition of  $(\text{Sn}_{0.2}\text{Ti}_{0.8})\text{O}_2$

Element	Calculated wt.%	Practical wt.%	% of error
Sn	25.248	24.76	1.932
Ti	40.723	39.59	2.782
O	34.028	30.58	10.132

### Dielectric property

The dielectric characteristics provide information about the electrical polarization, transport mechanism, structural change, effects of relaxation, and defects in the material. The relative permittivity ( $\epsilon_r$ ) and tangent loss ( $\tan\delta$ ) are two important fundamental factors of any dielectric material.  $\epsilon_r$  can be explained as the ability of a material to store energy, whereas  $\tan\delta$  characterizes the energy dissipation inside the dielectric because of the process of conduction and relaxation phenomena. Dielectrics are explored in different electronic applications depending on the values of  $\epsilon_r$  and  $\tan\delta$  at areas of various frequencies.  $\epsilon_r$  is a function of the capacitance and dimensions of a material as per the equation:

$$\epsilon_r = \frac{Ct}{A\epsilon_0}, \quad (4)$$

where  $C$ ,  $t$ ,  $A$ , and  $\epsilon_0$  are the material's capacitance, pellet thickness, cross-sectional area, and free space permittivity, respectively.

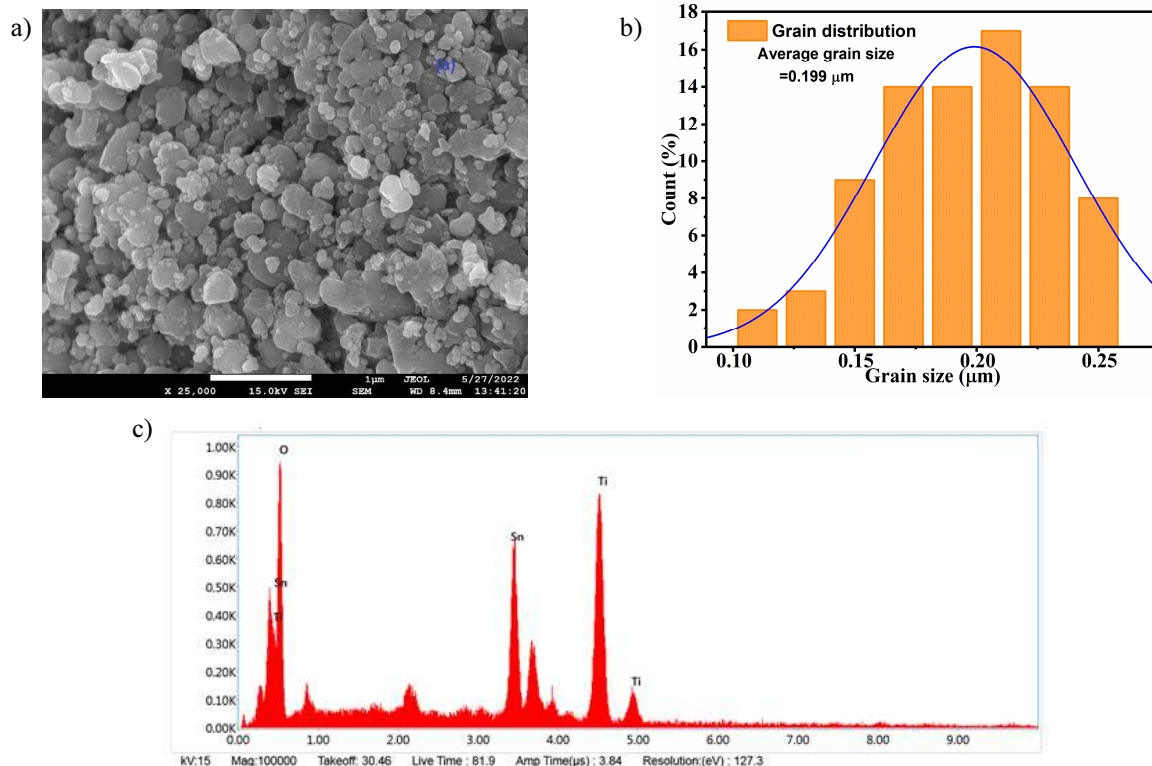


Fig. 3. SEM (a), grain distribution histogram (b) and EDAX (c) of  $(\text{Sn}_{0.2}\text{Ti}_{0.8})\text{O}_2$

The temperature vs.  $\epsilon_r$  graph at different frequencies is presented in Figure 4. The dielectric constant plot evinces a significant increase in  $\epsilon_r$  with temperature. It attains a peak at nearly 290°C (it may be indicated as the antiferroelectric-paraelectric phase transition) and the appearance of a peak at nearly 290°C demonstrates the thermally activated relaxation process in the studied composite [29, 30]. This sample exhibits an elevation of  $\epsilon_r$  with temperature due to space charge accumulation in the vicinity of the grain boundary. The relative permittivity also increases with temperature owing to the dominance of interfacial polarization on dipolar polarization. Similarly, Figure 5 presents the  $\tan\delta$  variation with temperature for different conditions of frequency. The  $\tan\delta$  peak for a certain temperature suggests the effect of space charge polarization. This effect may have arisen because of the two phases of grain-grain boundaries with various electrical conductivities [31, 32]. From the 1 kHz to 1 MHz rise in frequency, the loss value declines in the synthesized composite. The low loss value at higher temperatures for all the frequencies demonstrates the greater crystallinity nature of the material.

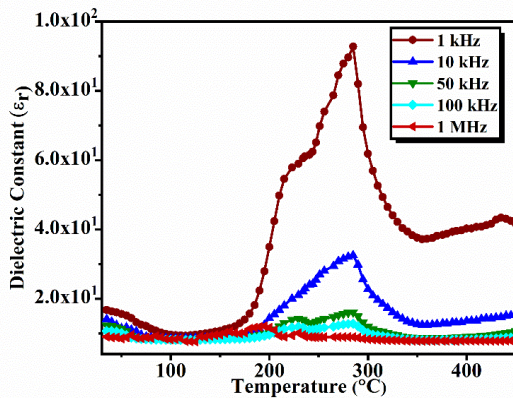


Fig. 4. Relative permittivity variation with temperature in  $(\text{Sn}_{0.2}\text{Ti}_{0.8})\text{O}_2$  for different frequencies

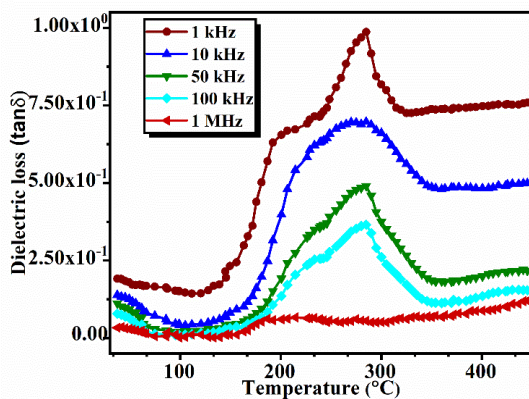


Fig. 5. Dielectric loss variation with temperature in  $(\text{Sn}_{0.2}\text{Ti}_{0.8})\text{O}_2$  for different frequencies

Figures 6 and 7 present the frequency response plots of  $\epsilon_r$  and  $\tan\delta$  respectively at different conditions of temperature. As the frequency increases,  $\epsilon_r$  at all the

temperatures exhibits a downward tendency and approaches a constant value when the frequency exceeds 100 kHz. Also,  $\epsilon_r$  increases with the temperature at the lower area of frequency, presenting the grain-boundary effect. It was observed that at 400°C the synthesized dielectric component achieved the highest  $\epsilon_r$  of 597 for a frequency of 1 kHz. This high  $\epsilon_r$  at low frequency and high temperature results mainly from the space charge at the grain boundaries [33]. Near the lower frequency zone, the  $\epsilon_r$  plot becomes dispersed, which corresponds to Maxwell Wagner-type polarization [34]. The dielectric constant starts to reduce with an increase in frequency because of the weakening of space charge polarization.

Similarly, as the frequency increases, the loss in tangent ( $\tan\delta$ ) decreases owing to the alignment of dipoles in the direction of the electric field. Nevertheless, as the frequency continues to rise, the dipoles become frozen, and the primary source of loss shifts to ionic vibrations in the higher frequency range. In contrast, at lower frequencies a higher  $\tan\delta$  is measured, which is associated with thermally energized carriers and unidentified material defects. For instance, at the elevated temperature of 400°C and the frequency of 1 kHz, an observed loss in tangent of 3.5 is recorded, which could potentially contribute to the improvement of the quality factor in applications involving fast electronic sensors. [35].

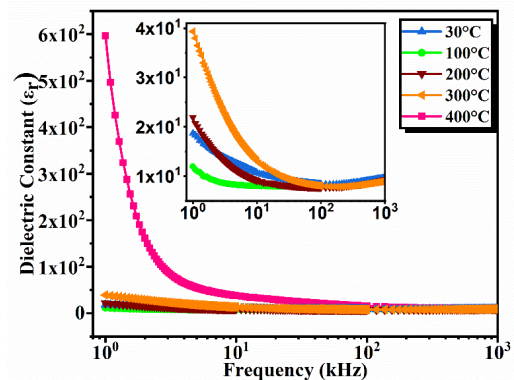


Fig. 6. Dielectric constant vs frequency of  $(\text{Sn}_{0.2}\text{Ti}_{0.8})\text{O}_2$  at selected temperatures

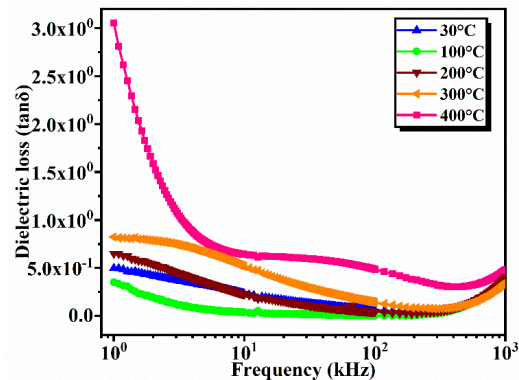


Fig. 7. Tangent loss vs frequency of  $(\text{Sn}_{0.2}\text{Ti}_{0.8})\text{O}_2$  at selected temperatures

## Impedance study

The different electrical properties with transport characteristics of the synthesized composite were evaluated by an impedance spectrometer. When the sintered pellet is subjected to an ac signal, phase shifting inside the material develops temporarily between the dipoles and driving field, resulting in polarization. The complex impedance  $Z^*$  relating to real  $Z'$  along with the imaginary  $Z''$  section can be expressed by the equation;  $Z^* = Z' - jZ''$ , where  $\frac{R}{1+(\omega\tau)^2}$  and  $\frac{\omega R\tau}{1+(\omega\tau)^2}$  are used to derive  $Z'$  and  $Z''$  respectively.

Figure 8 shows the frequency-dependent  $Z'$  plot at temperatures of 30–400°C. It was ascertained that the value of grain resistance  $Z'$  is high for both low frequency and temperature. As the frequency increases, the  $Z'$  curve tends to decrease and merge for frequencies greater than 100 kHz. This suggests the existence of space charge polarization specifically because of elevated temperatures and improvement of the semiconductor characteristics [36]. Also, the frequency relevance relaxation mechanism was ascertained from the resistive plot and the cause behind this occurrence is due to the oxygen vacancies [37, 38].

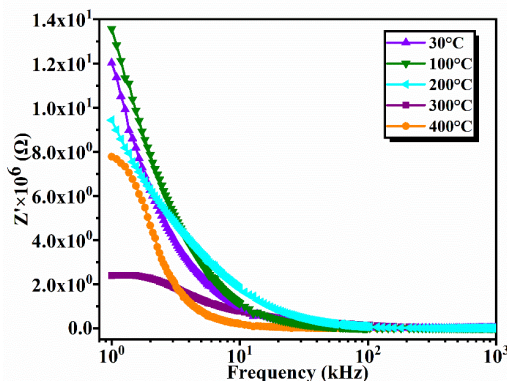


Fig. 8.  $Z'$  as a function of frequency across various temperatures

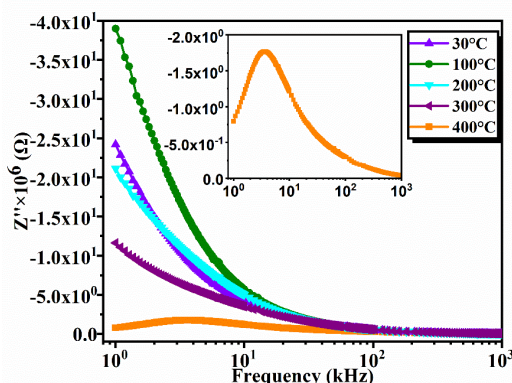


Fig. 9.  $Z''$  as a function of frequency across various temperatures

Figure 9 manifests the impedance loss spectrum ( $Z''$  vs frequency) and with growing frequency, a monotonically reducing curve of  $Z''$  at various temperatures is obtained. In the  $Z''$  spectrum, a peak appears at 400°C in the lower frequency zone and is called a relaxation

peak, which occurs due to grain boundaries. The presence of relaxation phenomenon is evinced with increased temperature in this studied dielectric. The exact frequency at which the  $Z''$  peak occurred is identified as the electrical relaxation frequency and from that particular peak height the bulk resistance of the material can be calculated.

## Conductivity study

When a dielectric material comes across an applied external field, conduction occurs because of the hopping of ionic charges between the nearby donors and acceptors. The ac conductance  $\sigma_{ac}$  is calculated using the mathematical formula:

$$\sigma_{ac} = 2\pi f \epsilon_r \epsilon_0 \tan \delta, \quad (5)$$

where all the symbols carry their usual meanings. Figure 10 depicts the  $\sigma_{ac}$  vs  $1000/T$  graph for the synthesized component  $(\text{Sn}_{0.2}\text{Ti}_{0.8})\text{O}_2$  for various frequencies. Initially,  $\sigma_{ac}$  falls between 35°C and 115°C, indicating that this component has a PTCR (positive temperature coefficient of resistance) feature. Between 115° and 245°C the conductivity rises, which can be called the NTCR effect (negative temperature coefficient of resistance), and thereafter decreases. The section on DC conductivity can be illustrated by the relation (Arrhenius equation) [39]:

$$\sigma_{dc} = \sigma_0 \exp\left[\frac{-E_a}{K_B T}\right], \quad (6)$$

where  $\sigma_0$ ,  $K_B$ , and  $T$  stand for the pre-exponential factor, Boltzmann constant, and temperature in Kelvin, respectively. The activation energies ( $E_a$ ) at all the selected frequencies are evaluated by linear fitting in the  $\sigma_{ac}$  vs  $1000/T$  graph and all the  $E_a$  data are noted in Table 2. It was observed that  $E_a$  reduces with frequency, which explains the thermal-activation relaxation mechanism in this composite ceramic material. When the frequency rises, the acceleration of charge carriers also increases, and hence they can freely jump to the nearest sites with less activation energy. The distinct values of the slopes in the conductivity graph in separate temperature ranges signify the multiple conduction processes in the material.

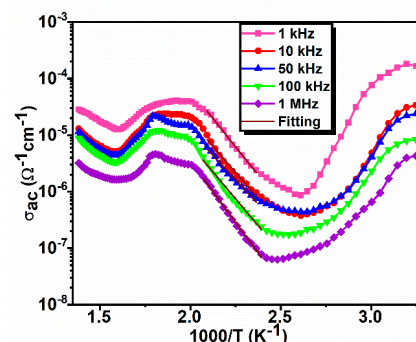


Fig. 10. Temperature-dependent ac conductivity at different frequencies in  $(\text{Sn}_{0.2}\text{Ti}_{0.8})\text{O}_2$

TABLE 2. Evaluated activation energy values in  $(\text{Sn}_{0.2}\text{Ti}_{0.8})\text{O}_2$  for selected frequencies

Frequency	$E_a$ [eV]
1 kHz	0.7922
10 kHz	0.7307
50 kHz	0.6874
100 kHz	0.6741
1 MHz	0.6602

### Complex modulus study

Additional information associated with relaxation phenomena, electrical conductivity, polarization, and the electrode effect in ionic conductors and ceramic materials can be investigated by modulus analysis [40]. The following mathematical statements are used to compute the real component  $M'$  and imaginary component  $M''$  of the electric modulus:

$$M' = A \left[ \frac{(\omega RC)^2}{1 + (\omega RC)^2} \right], \quad M'' = A \left[ \frac{(\omega RC)}{1 + (\omega RC)^2} \right],$$

$$\text{and } A = \frac{C_0}{C},$$

where  $\omega$  and  $C_0$  are the angular frequency and geometric capacitance, respectively. The variation in  $M'$  for a wide frequency range is presented in Figure 11. A very low value of  $M'$  was seen in the lower frequency section. As the frequency grows,  $M'$  also increases continuously and exhibits a sigmoidal shape near the higher frequency side, indicating short-range carrier mobility [41]. A low value of  $M'$  at the lowest frequency of 1 kHz at each temperature denotes a high  $\epsilon_r$  at that frequency.

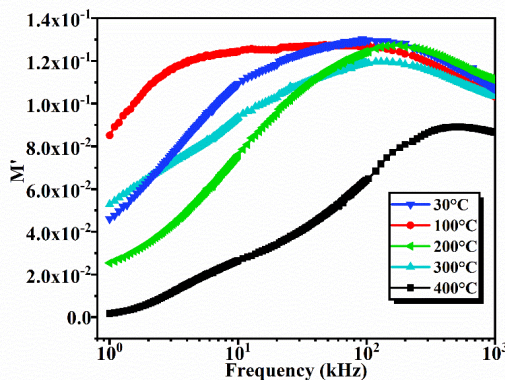


Fig. 11.  $M'$  as a function of frequency in  $(\text{Sn}_{0.2}\text{Ti}_{0.8})\text{O}_2$

The frequency-dependent  $M''$  graph at selected temperatures is exhibited in Figure 12. In the  $M''$  spectrum, initially the  $M''$  value increases with frequency, reaches a peak, and then dwindles. Except for 100°C, the peaks are shown at all temperatures as a consequence of fluctuations in the experimental data. The observation of peaks shifting towards higher frequencies with increased temperature is a common phenomenon in the

field of dielectric spectroscopy, and it suggests a thermally activated relaxation mechanism inside the dielectric material. The area where the  $M''_{max}$  peak occurs is referred to as the shifting of long to short-range carriers with enhanced frequency. This indicates the subsistence of the temperature-reliant hopping mechanism of the developed component. The broadened asymmetrical peaks of the studied composite exhibit non-Debye relaxation with improved relaxation time [42, 43].

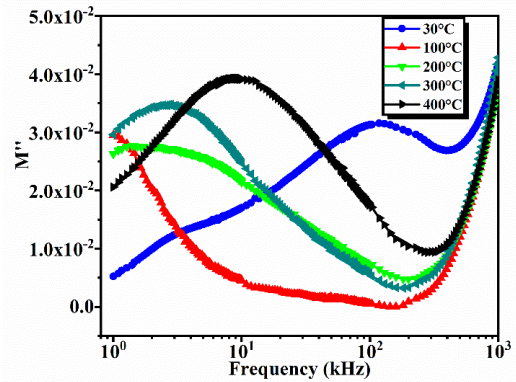


Fig. 12.  $M''$  as a function of frequency in  $(\text{Sn}_{0.2}\text{Ti}_{0.8})\text{O}_2$

### CONCLUSIONS

In this study, a solid-state method was used to create the ceramic composite  $(\text{Sn}_{0.2}\text{Ti}_{0.8})\text{O}_2$ . X'Pert HighScore Plus was used to perform structural analysis of the XRD data, and the results indicate that this component has a tetragonal crystal structure and an average crystallite size of 57.9 nm. The microstructural study performed using SEM and EDAX reveals an average grain size of 0.199  $\mu\text{m}$  as well as the theoretical and actual abundances of all the constituent components. The Maxwell-Wagner kind of dielectric dispersion was confirmed from the dielectric analysis. This sensor design element is motivated by the measurable low tangent loss. The conductivity study confirmed that the ceramic exhibits both PTCR and NTCR properties. This semi-conducting nature of the material is supported by its impedance characteristics. The modulus analysis proved that non-Debye relaxation occurred. Broadening of the modulus peak is evidence for the existence of several relaxations. Because of this, the synthetic composite electronic material can be investigated further as a possible component in electronic sensors operating at high temperatures.

### REFERENCES

- [1] He Z., Lyu Z., Gu Q., Zhang L., Wang J., Ceramic-based membranes for water and wastewater treatment, *Colloids and Surfaces A: Physicochemical and Engineering Aspects* 2019, 578, 123513, DOI: 10.1016/j.colsurfa.2019.05.074.
- [2] Colder H., Guilmeau E., Harnois C., Marinel S., Retoux R., Savary E., Preparation of Ni-doped ZnO ceramics for thermoelectric applications, *Journal of the European Ceramic*

- Society 2011, 31(15), 2957-2963, DOI: 10.1016/j.jeurceramsoc.2011.07.006.
- [3] Choi J.H., Kim Y.M., Park Y.W., Park T.H., Jeong J.W., Choi H.J., Song E.H., Lee J.W., Kim C.H., Ju B.K., Highly conformal  $\text{SiO}_2/\text{Al}_2\text{O}_3$  nanolaminate gas-diffusion barriers for large-area flexible electronics applications, *Nanotechnology* 2010, 21(47), 475203, DOI: 10.1088/0957-4484/21/47/475203.
- [4] Ates T., Tatar C., Yakuphanoglu F., Preparation of semiconductor ZnO powders by sol-gel method: Humidity sensors, *Sensors and Actuators A: Physical* 2013, 190, 153-160, DOI: 10.1016/j.sna.2012.11.031.
- [5] Shahraki M.M., Alipour S., Mahmoudi P., Karimi A., Novel multifunctional capacitor-varistor ceramics based on  $\text{SnO}_2$ , *Ceramics International* 2018, 44(16), 20386-20390, DOI: 10.1016/j.ceramint.2018.08.031.
- [6] Phule P.P., Risbud S.H., Low-temperature synthesis and processing of electronic materials in the  $\text{BaO-TiO}_2$  system, *Journal of Materials Science* 1990, 25, 1169-1183, DOI: 10.1007/BF00585422.
- [7] Das S.N., Relaxor  $(\text{Pb}_{0.7}\text{Bi}_{0.3})(\text{Mg}_{0.231}\text{Nb}_{0.462}\text{Fe}_{0.3})\text{O}_3$  electronic compound for magnetoelectric field sensor applications, *Journal of Applied Physics* 2020, 128, 114101, DOI: 10.1063/5.0014110.
- [8] Krishnakumar T., Jayaprakash R., Singh V.N., Mehta B.R., Phani A.R., Synthesis and characterization of tin oxide nanoparticle for humidity sensor applications, *International Journal of Nano Research* 2008, 4, 91-101, DOI: 10.4028/www.scientific.net/JNanoR.4.91.
- [9] Wang X., Sang Y., Wang D., Ji S., Liu H., Enhanced gas sensing property of  $\text{SnO}_2$  nanoparticles by constructing the  $\text{SnO}_2\text{-TiO}_2$  nanobelt heterostructure, *Journal of Alloys and Compounds* 2015, 639, 571-576, DOI: 10.1016/j.jallcom.2015.03.193.
- [10] Yawale S.P., Yawale S.S., Lamdhade G.T., Tin oxide and zinc oxide based doped humidity sensors, *Sensors and Actuators A: Physical* 2007, 135(2), 388-393, DOI: 10.1016/j.sna.2006.08.001.
- [11] Otitoju T.A., Okoye P.U., Chen G., Li Y., Okoye M.O., Li S., Advanced ceramic components: Materials, fabrication, and applications, *Journal of Industrial and Engineering Chemistry* 2020, 85, 34-65, DOI: 10.1016/j.jiec.2020.02.002.
- [12] Li W., Liu J., Ding C., Bai G., Xu J., Ren Q., Li J., Fabrication of ordered  $\text{SnO}_2$  nanostructures with enhanced humidity sensing performance, *Sensors* 2017, 17(10), 2392, DOI: 10.3390/s17102392.
- [13] Zhao Y., Yang B., Liu J., Effect of interdigital electrode gap on the performance of  $\text{SnO}_2$ -modified  $\text{MoS}_2$  capacitive humidity sensor, *Sensors and Actuators B: Chemical* 2018, 271, 256-263, DOI: 10.1016/j.snb.2018.05.084.
- [14] Sahoo L., Bhuyan S., Das S.N., Temperature-frequency dependent electrical properties of tin oxide-titania based capacitive electronic component, *Applied Physics A* 2022, 128, 1136, DOI: 10.1007/s00339-022-06264-8.
- [15] Sahoo L., Bhuyan S., Das S.N., Synthesis and electrical characterizations of  $(\text{Sn}_{0.8}\text{Ti}_{0.2})\text{O}_2$  electronic material, *Phase Transitions* 2023, 96, 1-14, DOI: 10.1080/01411594.2023.2219808.
- [16] Jarzebski Z.M., Morton J.P., Physical properties of  $\text{SnO}_2$  materials: III. Optical properties, *Journal of the Electrochemical Society* 1976, 123(10), 333C, DOI: 10.1149/1.2132647.
- [17] Zhang D., Sun Y.E., Li P., Zhang Y., Facile fabrication of  $\text{MoS}_2$ -modified  $\text{SnO}_2$  hybrid nanocomposite for ultrasensitive humidity sensing, *ACS Applied Materials & Interfaces* 2016, 8(22), 14142-14149, DOI: 10.1021/acsami.6b02206.
- [18] Tawale J.S., Gupta G., Mohan A., Kumar A., Srivastava A.K., Growth of thermally evaporated  $\text{SnO}_2$  nanostructures for optical and humidity sensing application, *Sensors and Actuators B: Chemical* 2014, 201, 369-377, DOI: 10.1016/j.snb.2014.04.099.
- [19] Nisiro D., Fabbri G., Celotti G.C., Bellosi A., Influence of the additives and processing conditions on the characteristics of dense  $\text{SnO}_2$ -based ceramics, *Journal of Materials Science* 2003, 38, 2727-2742, DOI: 10.1023/A:1024459307992.
- [20] Chenaina H., Messaadi C., Jalali J., Ezzaouia H., Study of structural, optical and electrical properties of  $\text{SnO}_2$  doped  $\text{TiO}_2$  thin films prepared by a facile sol-gel route, *Inorganic Chemistry Communications* 2021, 124, 108401, DOI: 10.1016/j.inoche.2020.108401.
- [21] Kim H.K., Sathaye S.D., Hwang Y.K., Jung S.H., Hwang J.S., Kwon S.H., Park S.E., Chang J.S., Humidity sensing properties of nanoporous  $\text{TiO}_2\text{-SnO}_2$  ceramic sensors, *Bulletin of the Korean Chemical Society* 2005, 26(11), 1881-1884, DOI: 10.5012/bkcs.2005.26.11.1881.
- [22] Chen Z., Lu C., Humidity sensors: a review of materials and mechanisms, *Sensor Letters* 2005, 3(4), 274-295, DOI: 10.1166/sl.2005.045.
- [23] Kumar V., Chauhan V., Ram J., Gupta R., Kumar S., Chaudhary P., Yadav B.C., Ojha S., Sulania I., Kumar R., Study of humidity sensing properties and ion beam induced modifications in  $\text{SnO}_2\text{-TiO}_2$  nanocomposite thin films, *Surface and Coatings Technology* 2020, 392, 125768, DOI: 10.1016/j.surfcoat.2020.125768.
- [24] Faia P.M., Furtado C.S., Ferreira A.J., Humidity sensing properties of a thick-film titania prepared by a slow spinning process, *Sensors and Actuators B: Chemical* 2004, 101(1-2), 183-190, DOI: 10.1016/j.snb.2004.02.050.
- [25] Das S.N., Pattanaik A., et al., Dielectric and impedance spectroscopy of Ni doped  $\text{BiFeO}_3\text{-BaTiO}_3$  electronic system, *Journal of Materials Science: Materials in Electronics* 2016, 27, 10099-10105, DOI: 10.1007/s10854-016-5084-2.
- [26] Sahoo L., Bhuyan S., Das S.N., Structural, morphological, and impedance spectroscopy of Tin oxide-Titania based electronic material, *Physica B: Condensed Matter* 2023, 654, 414705, DOI: 10.1016/j.physb.2023.414705.
- [27] Messaadi C., Ghrib T., Jalali J., Ghrib M., Alyami A.A., Gaidi M., Silvan M.M., Ezzaouia H., Synthesis and characterization of  $\text{SnO}_2\text{-TiO}_2$  nanocomposites photocatalysts, *Current Nanoscience* 2019, 15(4), 398-406, DOI: 10.2174/1573413714666180927110912.
- [28] Gay P.B., Hirsch P.B., Kelly A., The estimation of dislocation densities in metals from X-ray data, *Acta metallurgica* 1953, 1(3), 315-319, DOI: 10.1016/0001-6160(53)90106-0.
- [29] Barick B.K., Mishra K.K., Arora A.K., Choudhary R.N.P., Pradhan D.K., Impedance and Raman spectroscopic studies of  $(\text{Na}_{0.5}\text{Bi}_{0.5})\text{TiO}_3$ , *Journal of Physics D: Applied Physics* 2011, 44(35), 355402, DOI: 10.1088/0022-3727/44/35/355402.
- [30] Das S.N., Pradhan S.K., Kar D.P., Bhuyan S., Choudhary R.N.P., Excitation performance of fabricated PMN-BFO relaxor through electric field, *Journal of Materials Science: Materials in Electronics* 2018, 29, 9375-9379, DOI: 10.1007/s10854-018-8969-4.
- [31] Singh L., Rai U.S., Mandal K.D., Rai A.K., Effect of processing routes on microstructure, electrical and dielectric behavior of Mg-doped  $\text{CaCu}_3\text{Ti}_4\text{O}_{12}$  electro-ceramic, *Applied Physics A* 2013, 112, 891-900, DOI: 10.1007/s00339-012-7443-z.
- [32] Das S.N., Pradhan S., et al., Modification of relaxor and impedance spectroscopy properties of lead magnesium niobate by bismuth ferrite, *Journal of Electronic Materials* 2017, 46, 1637-1649, DOI: 10.1007/s11664-016-5207-9.

- [33] Sahoo L., Patnaik D., Bhuyan S., Das S.N., Structural, dielectric, and impedance spectroscopy investigation of titanium dioxide electronic system, *Materials Today: Proceedings* 2022, 67, 1159-1163, DOI: 10.1016/j.matpr.2022.07.330.
- [34] Prodromakis T., Papavassiliou C., Engineering the Maxwell-Wagner polarization effect, *Applied Surface Science* 2009, 255(15), 6989-6994, DOI: 10.1016/j.apsusc.2009.03.030.
- [35] Tripathy A., Pramanik S., Manna A., Azrin Shah N.F., Shasmin H.N., Radzi Z., Abu Osman N.A., Synthesis and characterizations of novel Ca-Mg-Ti-Fe-oxides based ceramic nanocrystals and flexible film of polydimethylsiloxane composite with improved mechanical and dielectric properties for sensors, *Sensors* 2016, 16(3), 292, DOI: 10.3390/s16030292.
- [36] Patnaik D., Nayak P.P., Bhuyan S., Das S.N., Structural, microstructural, and electrical behavior of a relaxor  $(Mg_{0.5}W_{0.5})(Pb_{0.5}Ni_{0.5})O_3$  electronic material, *Journal of the Australian Ceramic Society* 2023, DOI: 10.1007/s41779-023-00914-7.
- [37] Zhong M., Kumar N.P., Sagar E., Jian Z., Yemin H., Reddy P.V., Structural, magnetic and dielectric properties of Y doped  $BiFeO_3$ , *Materials Chemistry and Physics* 2016, 173, 126-131, DOI: 10.1016/j.matchemphys.2016.01.047.
- [38] Pradhan S.K., Das S.N., Halder S., Bhuyans S., Choudhary R.N., Dielectric dispersion and impedance spectroscopy of yttrium doped  $BiFeO_3$ - $PbTiO_3$  electronic system, *Journal of Materials Science: Materials in Electronics* 2017, 28, 9627-9633, DOI: 10.1007/s10854-017-6712-1.
- [39] Pradhan S.K., Das S.N., Bhuyan S., Behera C., Padhee R., Choudhary R.N., Structural, dielectric and impedance characteristics of lanthanum-modified  $BiFeO_3$ - $PbTiO_3$  electronic system, *Applied Physics A* 2016, 122, 1-9, DOI: 10.1007/s00339-016-0043-6.
- [40] Dhaou M.H., Hcini S., Mallah A., Bouazizi M.L., Jemni A., Structural and complex impedance spectroscopic studies of  $Ni_{0.5}Mg_{0.3}Cu_{0.2}Fe_2O_4$  ferrite nanoparticle, *Applied Physics A* 2017, 123, 1-9, DOI: 10.1007/s00339-016-0652-0.
- [41] Sagar R., Raibagkar R.L., Complex impedance and modulus studies of cerium doped barium zirconium titanate solid solution, *Journal of Alloys and Compounds* 2013, 549, 206-212, DOI: 10.1016/j.jallcom.2012.09.062.
- [42] Das S.N., Pradhan S.K., Bhuyan S., Choudhary R.N., Capacitive, resistive and conducting characteristics of bismuth ferrite and lead magnesium niobate based relaxor electronic system, *Journal of Materials Science: Materials in Electronics* 2017, 28, 18913-18928, DOI: 10.1007/s10854-017-7845-y.
- [43] Patnaik D., Nayak P.P., Bhuyan S., Das S.N., Temperature and frequency dependent dielectric and electrical properties of relaxor  $(Ca_{1/2}W_{1/2})(Pb_{1/2}Ni_{1/2})O_3$  electronic material, *Results in Chemistry* 2023, 5, 100991, DOI: 10.1016/j.rechem.2023.100991.